## 1.2 DUAL ION BEAM IRRADIATION STUDIES OF CAVITY EVOLUTION IN A TEMPERED MARTENSITIC STEEL AND NANOSTRUCTURE FERRITIC ALLOYS

— T. Yamamoto, Y. Wu, G. R. Odette (University of California, Santa Barbara), K. Yabuuchi, S. Kondo, A. Kimura (Kyoto University)

### OBJECTIVE

The objective of this work is to characterize cavity evolution under $Fe^{3+}$ and $He^{+}$ dual ion beam irradiation in a normalized and tempered martensitic steel (TMS) F82H mod.3 and two nanostructured ferritic alloys (NFA), MA957 and 14YWT-PM2.

### SUMMARY

Dual ion ($Fe^{3+}$ and $He^{+}$) irradiations (DII) were performed at 500°C and 650°C, to nominal dpa and He levels of ≈ 10 to 47 dpa and ≈ 400 to 2000 appm, respectively. The irradiations were performed at dual ion beam facility, DuET, located at Kyoto University in Japan. The actual dpa, He and He/dpa vary with depth. The alloys studied include normalized and tempered martensitic steel, (TMS) F82H mod.3 (at 500°C), and two nanostructured ferritic alloys (NFAs), MA957 (at 500 and 650°C) and 14YWT-PM2 (at 650°C). The dual ion results are compared to in situ He injection (ISHI) irradiations in HFIR at a much lower dpa rate. The cavity microstructures were characterized by TEM. Cavities in the DII were observed at depths up to ≈ 1600 nm. The TMS F82H irradiated at 500°C contains a moderate density of non-uniformly distributed cavities with sizes ranging from ≈ 1 nm up to ≈ 20 nm, including large faceted voids along with small bubbles. In contrast, the MA957 contains a uniform distribution of small ≈ 1.3 nm diameter bubbles. Notably a similar bubble distribution is observed up to ≈ 80 dpa and ≈ 3900 appm He at 650°C, demonstrating the outstanding He management capability of nm-scale features in MA957 and 14YWT. The net swelling in F82H at 500°C reaches ≈ 0.29% at 45 dpa, with a well-established post-incubation population of growing voids. Swelling is also observed in the ISHI irradiations, which manifest even more pronounced bimodal cavity size distributions compared to those for DII conditions. Notably, the incubation dose (He and dpa) for swelling appears to be shifted too much lower dpa in the ISHI case, and the swelling rate appears to be higher. While the absolute swelling and swelling rates are low in both cases, it is important to emphasize that it is likely that the cavity volume fraction will continue to increase, and even accelerate, at higher dpa, perhaps reaching the nominal 0.2%/dpa proposed by Garner. In contrast the bubbles in the NFA are very similar in all cases, even for the DII at 650°C.

### PROGRESS AND STATUS

#### Introduction

Predicting and mitigating the effects of a combination of large levels of transmutant He and displacement damage (dpa), produced by high energy neutrons, on the dimensional stability

and mechanical properties of structural materials is one of the key challenges in the development of fusion energy [1]. The fundamental overriding questions about He-dpa synergisms include: a) what are the basic interacting mechanisms controlling He and defect transport, fate and consequences, and how are they influenced by the starting microstructure and irradiation variables (dpa rate, He/dpa ratio, temperature and applied stress)? and, b) how can the detrimental effects of He-dpa synergisms be mitigated and managed by proper microstructural design?

We have previously demonstrated that in situ He implantation (ISHI) in mixed spectrum fission reactor irradiations provides a very attractive approach to assessing the effects of He-dpa synergisms, while avoiding most of the confounding effects associated with Ni- or B-alloy doping type experiments [1-8]. Another approach is to use multiple ion beams to simultaneously implant He and create displacement damage with heavy ions [1,9-12]. In spite of an apparent similarity, however, the two techniques manifest many differences that include the dpa rates, the spatial distribution of dpa and He and the proximity of a free surface in the case of DII. Thus comparing the microstructural evolutions in the same alloys for the two different irradiation techniques is an important objective, and provides a basis to inform, calibrate and validate predictive models.

**Experimental Procedure**

The alloys studied here are a TMS F82H mod.3 and two NFAs, MA957 and 14YWT-PM2. The F82H series is a TMS alloy widely used for variety of studies, including characterizing He effects [1,3,7,11-17]. In the case of F82H mod.3, the base composition of F82H-IEA (nominally wt.%, 7.5%Cr 2%W 0.2%V 0.1%C 0.1%Si 0.02%Ta, 60ppm N, bal. Fe) was modified to reduce N and Ti to 14 ppm and 0.001%, respectively, while adding 0.1% Ta [13]. The steel was austenitized at 1040°C for 30 min, normalized (air-cooled), and tempered at 740°C for 1.5 h. F82H mod.3 has a fine prior-austenite grain size (ASTM 9.5) containing packets of finer scale lath structures formed during the martensitic transformation [13]. It also contains carbide precipitates over a wide range of sizes. MA957 is a representative of the 14YWT NFA (nominally Fe-14%Cr, 1%Ti, 0.3%Mo, 0.25$Y_2O_3$, bal. Fe) ferritic stainless steel that was produced by INCO in the late 1970s and 1980s. NFA are of growing interest due to their radiation damage resistance, and especially good He management capabilities; NFAs also have outstanding high temperature mechanical properties [1,5,8,18,19]. As-extruded MA957 has a fine scale elongated grain structure containing nm-scale oxide nanofeatures (NFs) dispersed in the matrix; the NFs act as obstacles to dislocation glide and climb. The average grain size ($d_g$) in MA 957 is about 1 and 5 mm in the transverse and axial directions, respectively. The number densities (N) and average diameter (<d>) of the NFs in MA957 are ≈ $5.3\times10^{23}/m^3$ and 2.7 nm, respectively. The corresponding dislocation densities (r) are ≈ $0.8\times10^{15}/m^2$. The PM2 14YWT NFA heat (nominally Fe-14%Cr, 3%W, 0.35%Ti, 0.3%$Y_2O_3$ wt.%, bal. Fe) was produced at ORNL by D. Hoelzer as part of a LANL-ORNL-UCSB collaboration to develop a larger, best practice heat of 14YWT. The N, d, $d_g$ and r in PM2 are ≈ $8\times10^{23}/m^3$, 1.8 nm, 425 nm and $1.2\times10^{15}/m^2$, respectively. More details about these materials, including processing paths, micro-nanostructures and properties, are given elsewhere [5,13,18,19].

The specimens used in the 500°C irradiations were 3 mm diameter disks mechanically ground to a nominal thickness of 200 mm, while 4 x 8 (mm) coupons with a nominal thickness of 500 mm were used for the 650°C irradiation. The specimen surfaces were electro-polished before irradiation. The DII was performed in DuET facility in the Institute of Advanced Energy, Kyoto University (Kyoto, Japan), where $Fe^{3+}$ ions are accelerated to 6.4MeV by a tandem accelerator and $He^{+}$ ions are accelerated to 1MeV by a single end accelerator. The specimens were positioned in a temperature-monitored/controlled stage [20]. The $He^{+}$ ion beam was passed through a rotating beam energy degrader creating four ion implantation energy bands, that result in a broader and more uniform He deposition profile up to a maximum depth of ≈ 1500 nm.

The 500°C irradiations targeted nominal conditions at 600 nm from the specimen surface of 10 dpa/400 appm He and 25 dpa/1000 appm He. The 650°C DII targeted a nominal condition at 600 nm of 48 dpa and 2200 appm. Table 1 summarizes the irradiation conditions, while Figure 1 shows depth profile of the dpa damage and He deposition calculated with SRIM 2006 code for the 650°C case. As can be seen in the profile the implantation covers a wide range of He, He/dpa ratios, dpa and dpa rates. The region between ≈ 400 to 1100 nm has an approximately constant He/dpa ratio of ≈ 48±5 appm/dpa. Near the He peak at ≈ 1050 nm, the displacement dose is ≈ 83 dpa and the He concentration is ≈ 3900 appm. The corresponding dpa rates are ≈ 1 and 1.7 $x10^{-3}$ dpa/s for 650 °C, and ≈ 5 and 9 $x10^{-4}$ dpa/s for the 500°C irradiations. More generally, the dpa increases to a peak at ≈ 3 times the nominal dose at 1600 nm, while the He and He/dpa decrease with increasing depths greater than 1100 nm, approaching 0 at ≈1500 nm. Thus, in principle, a DuET irradiation provides a basis to evaluate the effects of a wide range of irradiation dose variables, including high dpa with no He, as well as undamaged regions. The target specimen temperature was maintained by resistive heating of the stage that adjusts for the ion beam heating.

Table 1. Summary of DuET experimental conditions.

| Exp ID | Materials | T (°C) | Nominal Condition (@550-650nm) | | | | Peak He (@1000-1100nm) | | |
|---|---|---|---|---|---|---|---|---|---|
| | | | dpa | He (appm) | He/dpa | dpa/s | dpa | He (appm) | He/dpa |
| DI10B1 | F82H mod.3, MA957 | 500 | 25 | 1010 | 40 | $5.0 \times 10^{-4}$ | 43 | 1750 | 40 |
| DI10B3 | | | 10.1 | 406 | 40 | $5.1 \times 10^{-4}$ | 17 | 700 | 40 |
| DI12A1 | MA957, 14YWT(PM2) | 650 | 48 | 2230 | 47 | $1.1 \times 10^{-3}$ | 83 | 3860 | 47 |

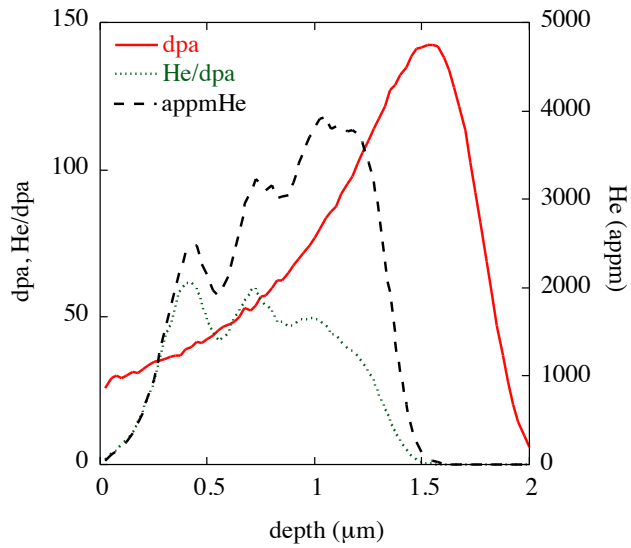


Figure 1. Depth profile of displacement damage and He deposition in the specimens in the DuET dual ion beam irradiation calculated with SRIM 2006 code for the case of nominal 47 dpa irradiation.

A FEI HELIOS Focused Ion Beam (FIB) tool was used to micro-machine < 100 nm thick electron transparent ≈ 5 mm wide and 5 mm deep lift-outs that included both damaged-implanted and undamaged regions. TEM was performed on the FEI 200 keV Technai T20 and 300 KeV Titan instruments in the UCSB Microstructure and Microanalysis Facility. Through focus bright field imaging was used to characterize the cavities. The cavity images were manually marked for location and size, and the image analysis software package Image-J was used to determine their area number densities and size distributions. The foil thickness, needed to compute volume number densities, was measured by convergent beam electron diffraction.

## RESULTS

*Cavity formation in TMS F82H and NFA MA957 after nominal 25dpa/1000appm He irradiation at 500°C*

Figures 2a-b show the TEM images for irradiated (a) F82H mod.3 and (b) MA957 around 1000 nm from the surface, at an estimated 43 dpa and 1750 appm He. Note that the magnification is adjusted to provide the best visibility for each alloy. The F82H mod 3 contains a moderate number density (N) of cavities over a wide range of diameters (d), from ≈ 1 to ≈ 20 nm. In this case the cavities are non-uniformly distributed, in a way that depends on the local microstructure. In contrast, the size and spatial distributions of He bubbles in MA957 are more uniform, with larger N and smaller d. The average diameter (<d>) of the cavities in F82H mod3 varies with depth and ranges up to <d> ≈ 5.0 nm, while in MA957 <d> ≈1.3 nm.

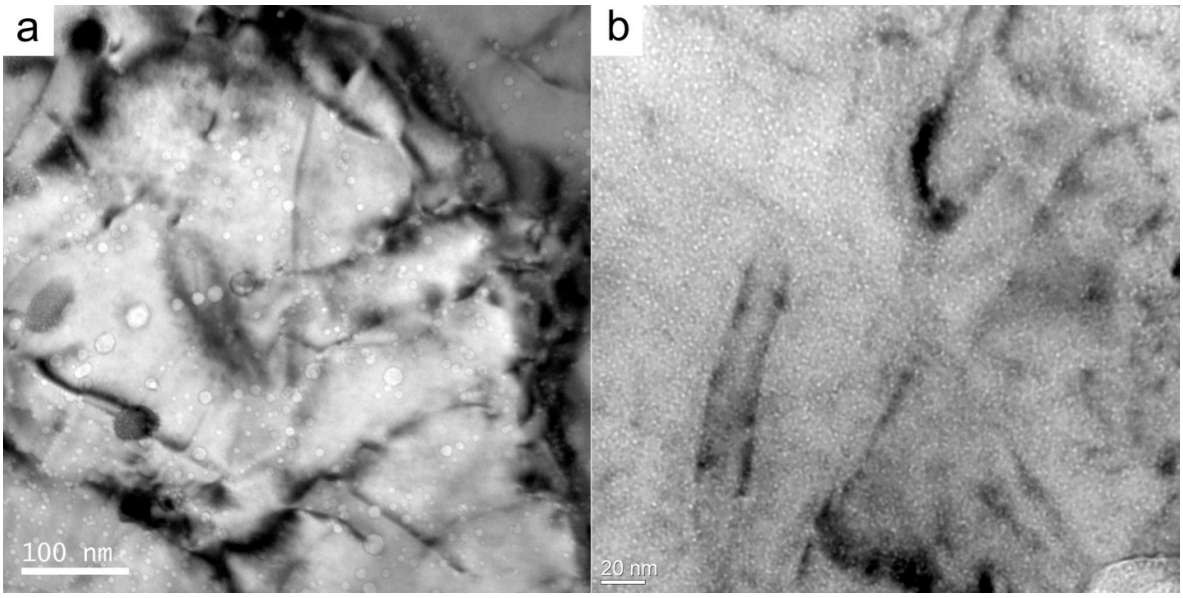


Figure 2. Under-focused bright field TEM images of the DII cavity structures in nominal 25 dpa, 500°C condition in (a) F82H mod3 and (b) MA957 that produced ≈ 43 dpa and 1750 appm He at ≈1000 nm from the surface.

Figure 3 shows N and <d> as a function of the depth greater than 600 nm. The N ranges from < 1 to ≈ $5x10^{22}/m^3$ in F82H; the corresponding <d> ranges from ≈ 3 to ≈ 5 nm, and systematically increases with the amount of implanted He and dpa. The <d> in MA957 is almost constant at ≈ 1.3 nm, while N ranges from ≈ 2.5 to $5x10^{23}/m^3$. These results clearly demonstrate the superior He management capability of the NFA compared to TMS. Note the spatial variations in N are not systematic, especially in F82H; again this is believed to be largely due to the effects of locally non-uniform microstructures that act as the bubble formation sites.

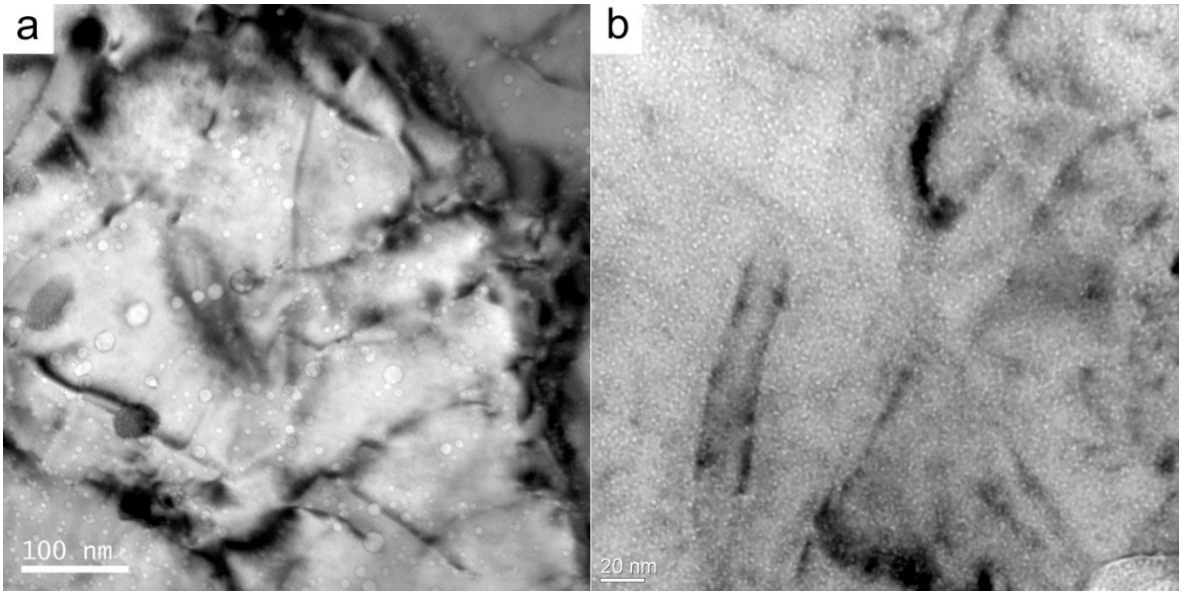


Figure 3. Average size and number density of cavities as a function of depth for the DII at 500°C in the nominal 10 dpa and 400 appm He condition in: (a) F82H mod.3; and, (b) MA957.

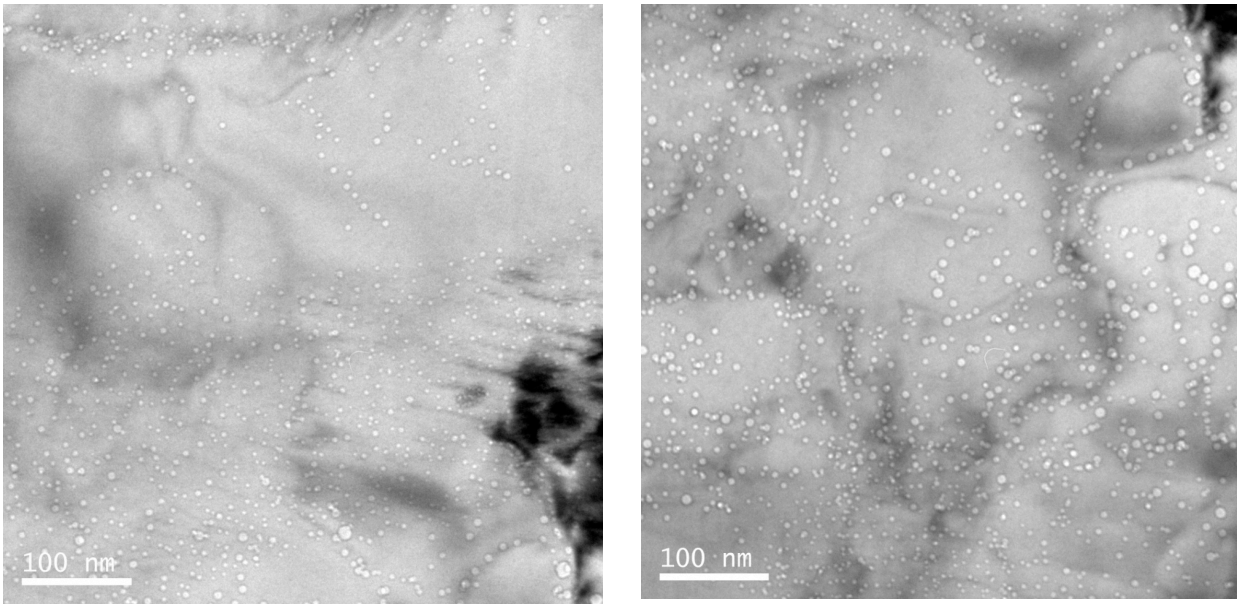


Figure 4. Cavity microstructures in F82H mod.3 irradiated to nominal 25 dpa at 500°C at two depths, (a) 0.5 to 1.0mm and (b) 0.9 to 1.4 mm. The dpa and He at the vertical center of the picture are ≈ 30 and ≈ 50 dpa, and ≈ 1200 and 2000 appm, respectively.

Figure 4a and b illustrate the cavity microstructure in F82H mod.3 irradiated to nominal 25 dpa at two depths, from the top edge to the bottom of the micrographs of: (a) 500 to 1000 nm and (b) 900 to 1400 nm. The dpa and He at the vertical center of the micrographs are ≈ 30 dpa/1200 appm and ≈ 50 dpa/2000 appm, respectively. The higher dpa and He leads to increased average cavity size <d> and especially more numerous larger faceted voids.

Figure 5 plots of the corresponding variations of N, <d> and the volume fraction (f) of cavities as a function of the He (a,d,g) and dpa (b,e,h). He/dpa (c,f,i) and He*dpa (j,k,l) for depths between 650 and 1250 nm. The various measures of damage were derived from the profiles shown in Figure 1, scaled to the actual He and dpa for each data set. The dependence of N on He, dpa and He/dpa is weak. The <d> and f do not vary systematically with He/dpa, but tend to increase with He and dpa. Here we focus on the cavity trends as a function of He(appm)*dpa, which provides the best correlation of the swelling (f) trends (Fig. 5j-l). Note, there is no special significance in the use of this damage parameter, except that both He and dpa are needed for void formation. The variation of N in F82H with He*dpa is not systematic but appears to decrease slightly at higher He*dpa. However, the overall trends of increasing <d> and f are very clear. Bubbles in the 10 dpa and 400 appm He data set dominate the cavity microstructure, but the small increases in <d> and f indicate the slow conversion of some bubbles to voids. The increases in the <d> and f with He*dpa are clear in the higher 25 dpa and 1000 appm He data set. The trend in f is approximately linear beyond a threshold He*dpa, except for the highest combined damage points, which have the highest dpa but a lower and He and He/dpa ratio. These figures also include 500°C data (open symbols) for several TMS alloys from in situ helium injection (ISHI) irradiation experiment for the data sets at 9 dpa/380 appm He and 21.2 /1230 appm He. The transition to void swelling is much faster in the ISHI case, perhaps due to the much lower fusion relevant damage rates. The swelling rates are also higher.

Figure 6a and b plot the cavity size distribution for the peak He in the DII irradiation and for a 500°C ISHI to 530 appm He/21.2 dpa [21]. Clearly the formation and evolution of larger voids occurs at lower He and dpa levels in the ISHI case.

Figure 7 shows the same plots as in Figure 5 but for MA957. Clearly the trends are very different than in the F82H. In MA957 the <d> are remarkably constant, while the N and f appear to decrease with He*dpa. The N in MA957 are much higher and the <d> much smaller than in F82H. These results clearly indicate the ability of NFs in NFA to manage high concentrations of He.

*Cavity formation in NFA MA957 and 14YWT(PM2) after nominal 48 dpa irradiation at 650°C*

Figures 8 a-b show the under- and over-focus images of MA957 for the 650°C DII at around 600 nm, with 48 dpa/2200 appm He. Figure 8c-d show the corresponding images for 14YWT-PM2. Figure 9a-d show the corresponding set of images near 1050 nm with ≈ 83 dpa/3800 appm He. The red lines mark increasing depth in 100 nm increments. In spite of these extremely severe damage conditions, the high N is generally similar to those shown in Figure 2 that are at much lower dpa and He levels. The <d> of the bubbles is nearly the same in both locations, while number density depends strongly on the amount of injected He. There is no evidence of void formation. He bubbles are observed on a grain boundary in the region with 83 dpa/3800 appm. These bubbles appear to be larger than those in the matrix. However it is not clear if the individual bubbles themselves are larger, or if this is the result of the larger grain boundary NFs that the bubbles are associated with. Indeed, a number of bubbles are observed to decorate

larger precipitates. Thus it is possible that small bubbles may coalesce on the interface forming a larger NF cavity.

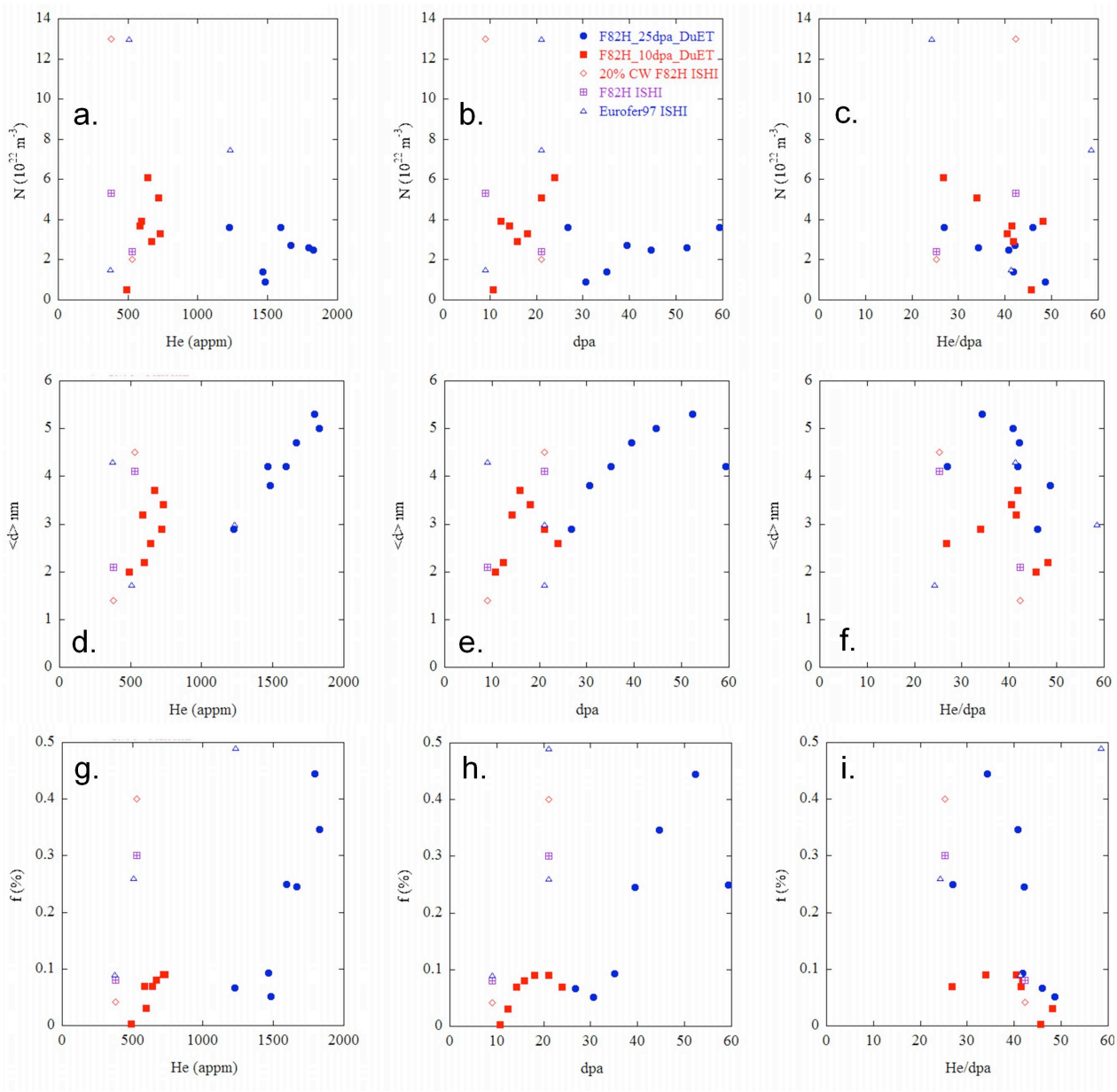


Figure 5a-i. The N, <d> and f of cavities as a function of the He (a,d,g), dpa (b,e,h) and He/dpa (c,f,i) for DII at depths between 650 and 1250 nm in F82H mod.3 irradiated at 500°C to a nominal 10 and 25 dpa (filled symbols). The DII results are compared with three ISHI irradiated TMS alloys, F82H mod.3 (as tempered and 20% cold worked conditions) and Eurofer97 ISHI experiments (unfilled symbols).

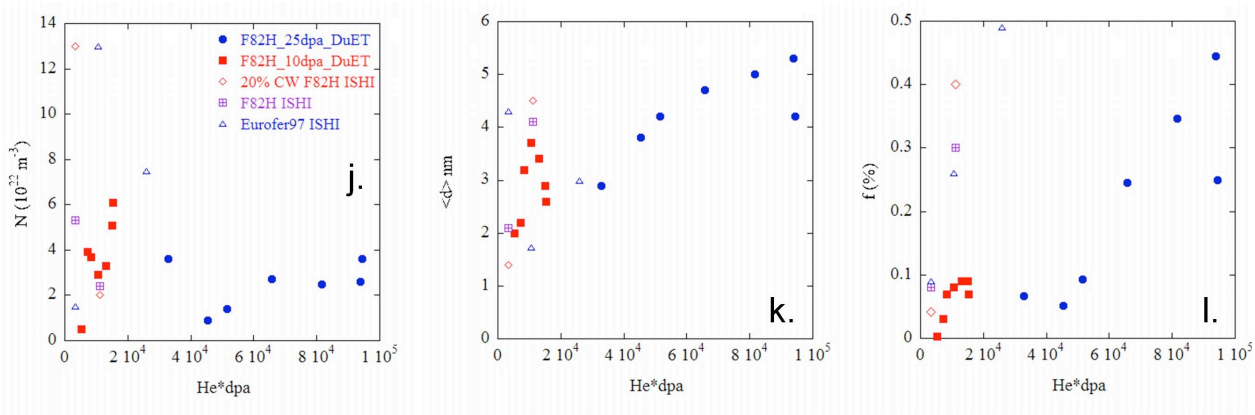


Figure 5j-l. The N, <d> and f of cavities as a function of the He(appm)*dpa at depths between 650 and 1250 nm nm in F82H mod.3 DII at 500°C to a nominal 10 and 25 dpa, compared with three ISHI irradiated TMS alloys, F82H mod.3 (as tempered and 20% cold worked conditions) and Eurofer97.

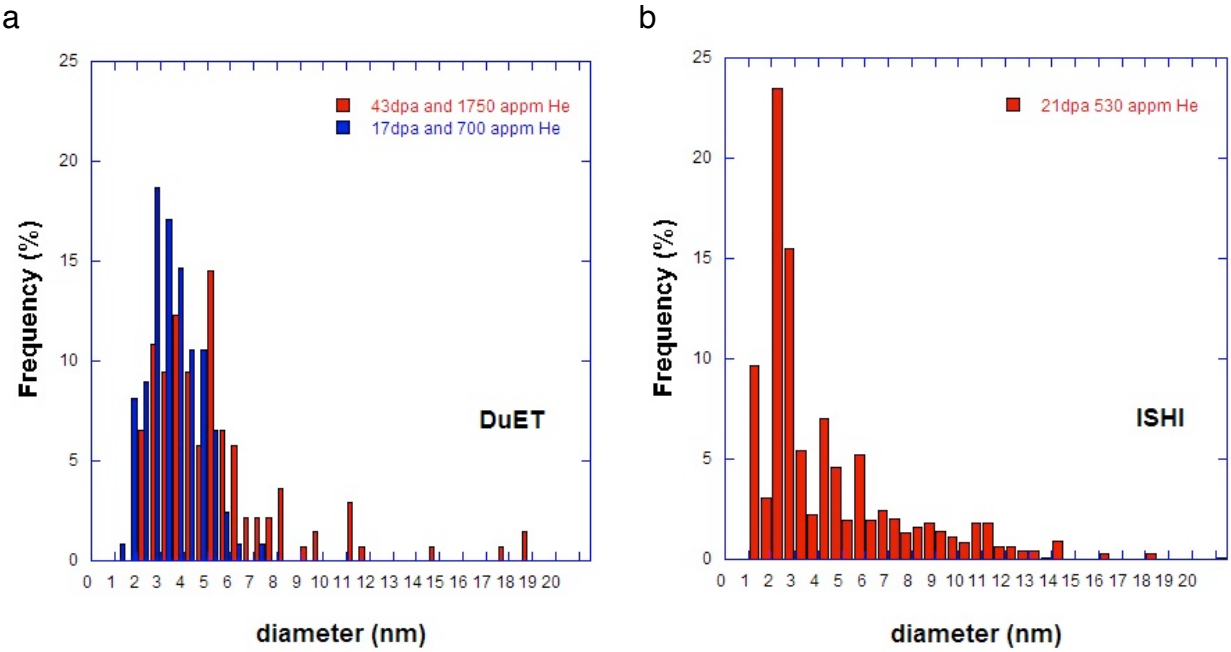


Figure 6. Cavity size distributions in F82H mod. 3 irradiated at 500°C in (a) in DuET and (b) in HFIR ISHI experiments to the indicated dpa and He levels.

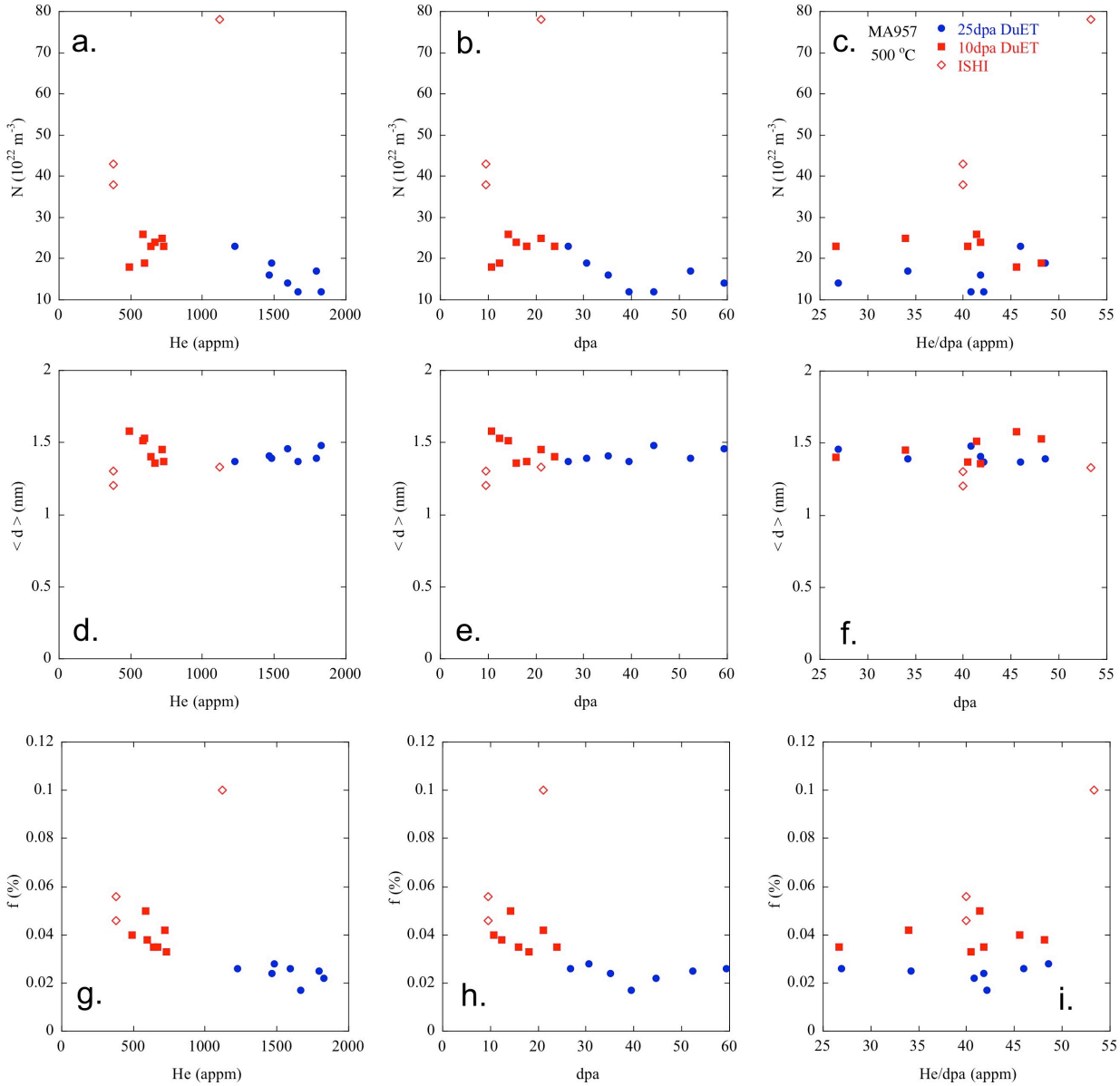


Figure 7a-i. The N, <d> and f of cavities as a function of the He (a,d,g), dpa (b,e,h) and He/dpa (c,f,i) for DII at depths between 650 and 1250 nm in MA957 irradiated at 500°C to a nominal 10 and 25 dpa (filled symbols) compared ISHI irradiated MA957 (unfilled symbols).

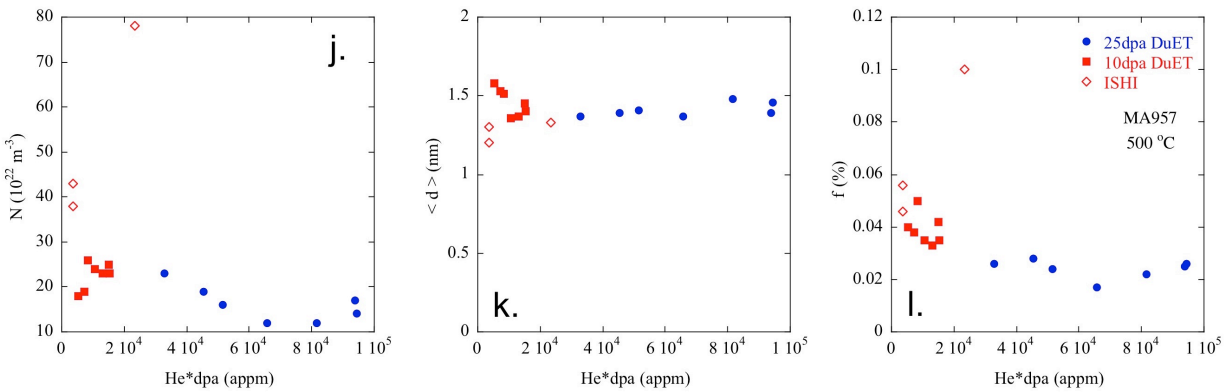


Figure 7 j-l. The N, (b), <d> and f of cavities as a function of the He(appm)*dpa at depths between 600 and 1200 nm in MA957 DII at 500°C to a nominal 10 and 25 dpa, compared ISHI irradiated MA957 (open symbols).

*Cavity formation in NFA MA957 and 14YWT(PM2) after nominal 48 dpa irradiation at 650 °C*

Figure 10a-b summarizes the average cavity size and number density as a function of depth in (a) MA957 and (b) 14YWT-PM2, respectively. Figure 11 compares the estimated amount of He that can be accounted for in the bubbles based on the observed size distributions and number densities compared to TRIM estimates of the total injected He. There is a large discrepancy that is not understood. Potential reasons include underestimating the size of small bubbles, unaccounted for He that contained in even smaller unresolved bubbles, or those that are hidden by the associated NFs, uncertainties in the bubble surface energy and the He equation-of-state (EOS), although in the latter case the He is probably underestimated. The reasons for these differences continue to be under active investigation. Figure 12 shows the narrow size distribution of matrix bubbles in both NFA at the nominal and peak He regions. Figure 13 plots the N, <d>and f for the DII of the NFA at 650°C as a function of He, dpa, He/dpa and He*dpa, similar to those shown previously. The most notable results are that <d> is independent of He*dpa, while the corresponding N and, especially, f increase. The observed bubble f is higher in MA957 than in 14YWT-PM2.

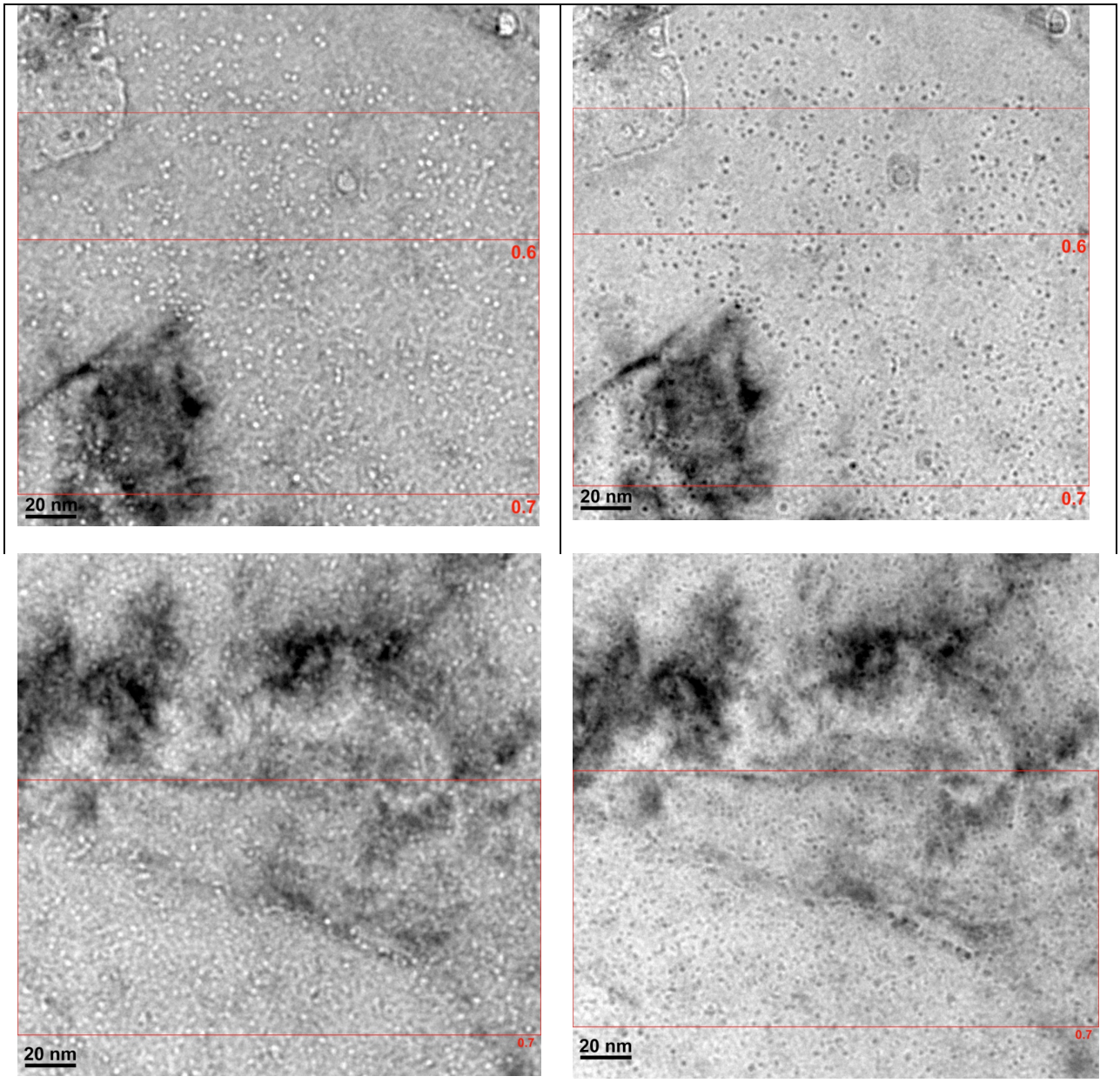


Figure 8. Under- and over-focus images of MA957 and 14YWT PM2 DII at 650°C to ≈ 48 dpa/2200 appm He.

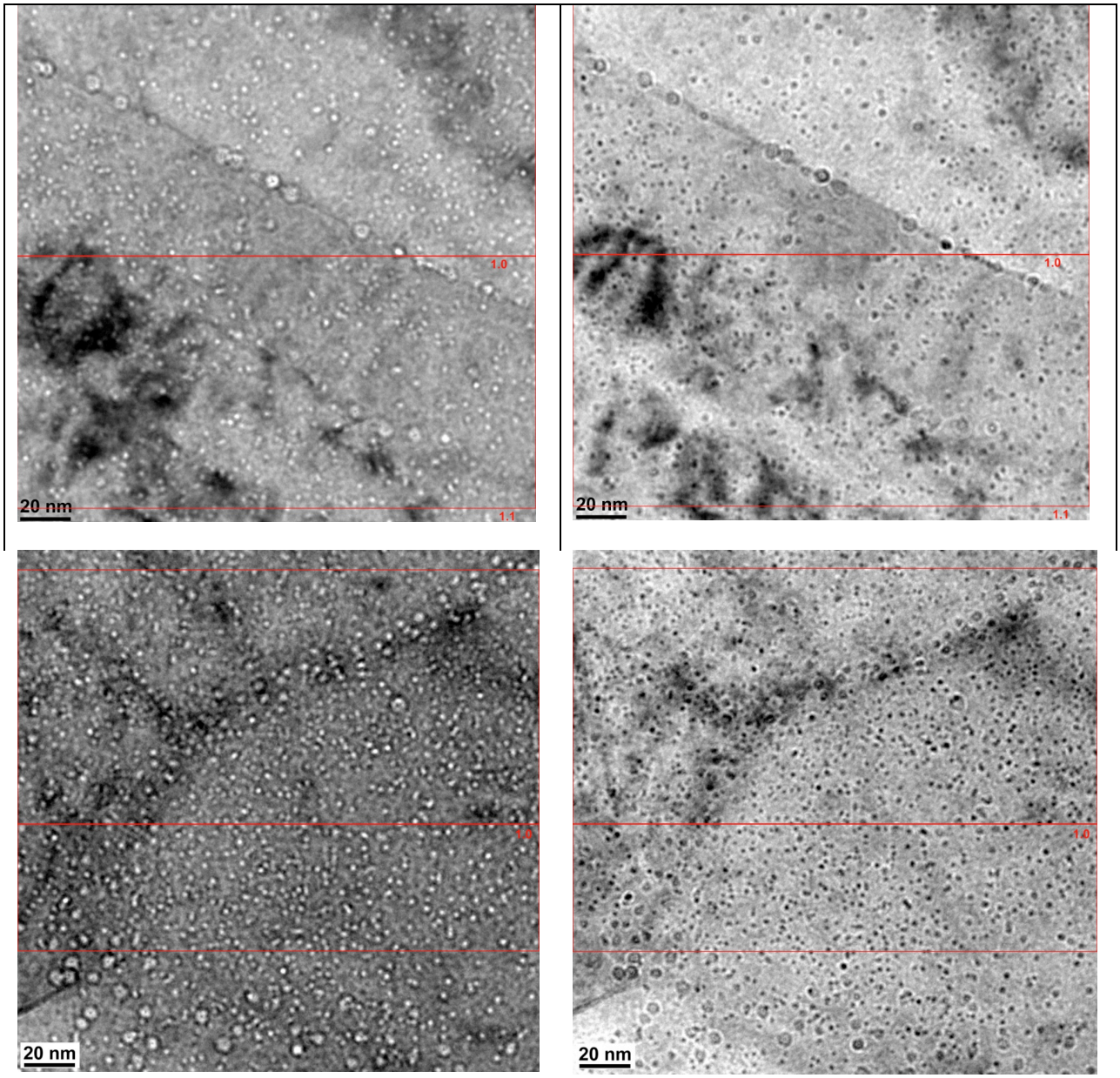


Figure 9. a) Under- and b) over-focus images of MA957 and 14YWT PM2 DII at 650 °C,to ≈ 83 dpa/3800 appm He.

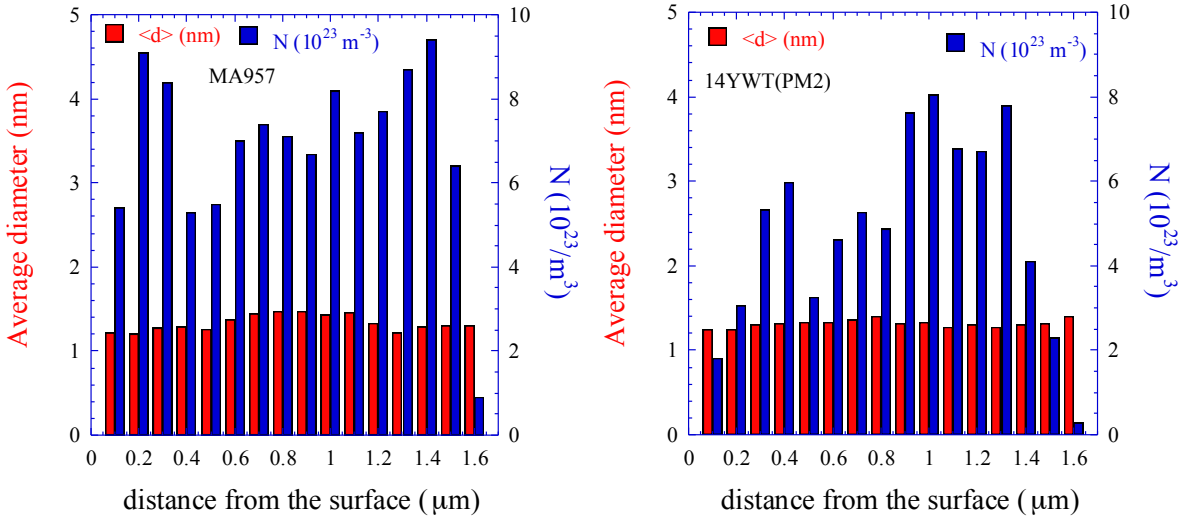


Figure 10. Average cavity size and number density as function of depth in the MA957 and 14YWT PM2 DII at 650°C.

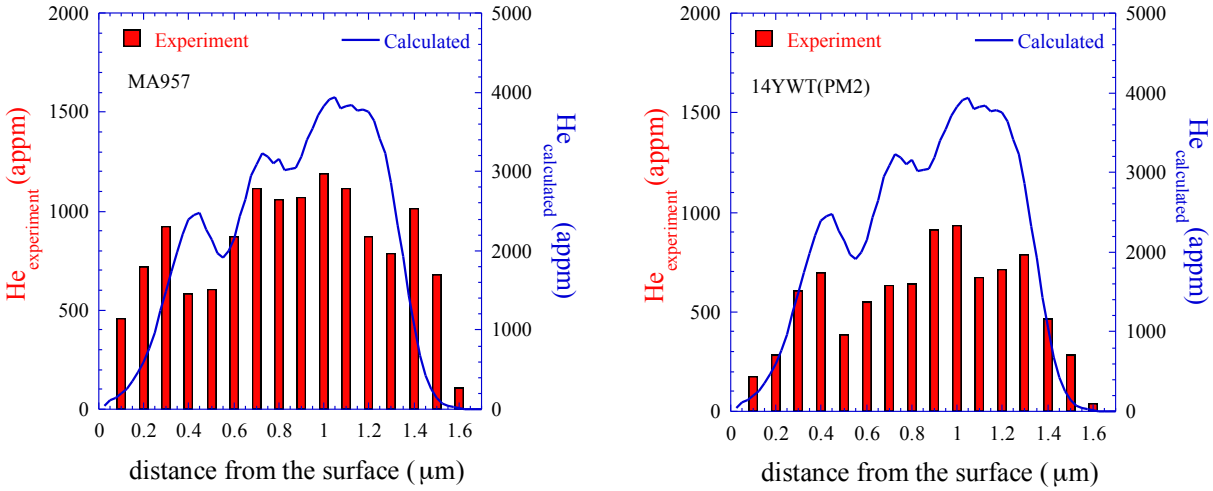


Figure 11. The estimated He in bubbles as a function of depth compared to the injected amount as calculated by TRIM for the 650°C DII.

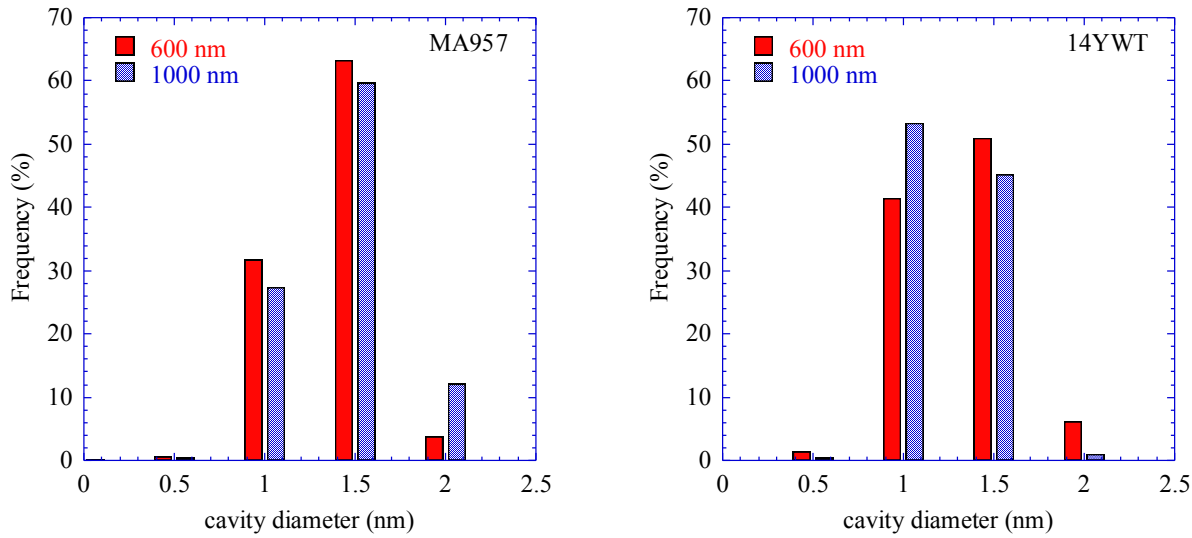


Figure 12. Cavity size distribution at nominal and peak He locations in the DII at 650°C.

## DISCUSSION AND FUTURE RESEARCH

Figure 14 cross-compares plots of N, <d> and f versus He*dpa for the different irradiation conditions, illustrating the basic differences between cavity evolution in TMS F82H mod.3 and NFA MA957 and 14YWT PM2, including at 650°C in the case of MA957 and 14YWT PM2. The key observations include:

The N are generally weakly dependent on He*dpa.

The NFA contain a much higher N and smaller <d> and f, since the cavities in this case are all bubbles, compared to the TMS, which contain a mixture of small bubbles and larger voids.

The bubbles in NFA are associated with the large number of NFs.

A small but systematic increase in f (swelling) begins in the TMS beyond He*dpa ≈ $5x10^4$ appm He-dpa due to the presence of growing voids, as signaled by a corresponding trend in <d>.

The <d> in the NFA are essentially independent of He*dpa and the DII temperature.

The N and f in the NFA increase with He*dpa and the DII temperature.

The objective of this report was to summarize the DII results and to crudely assess trends in the cavity microstructures with various measures of irradiation dose. However, this significant and growing database, and the corresponding results for the ISHI, will provide a very rich knowledge base for more detailed analysis and modeling studies in the future.

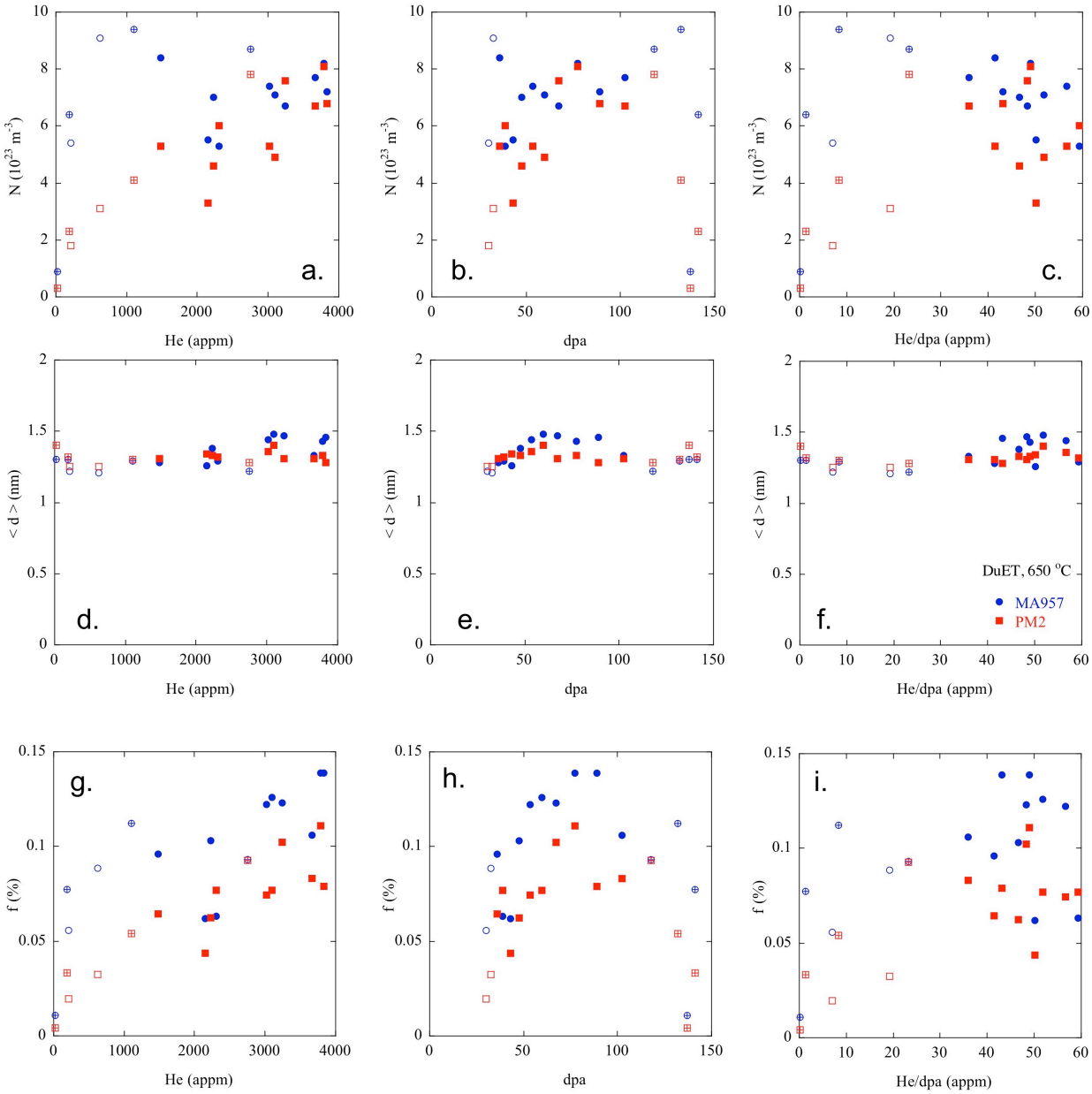


Figure 13. The N, <d> and f of cavities as a function of the He (a,d,g) and dpa (b,e,h). He/dpa (c,f,i) for depths between 100 and 1600 nm in MA957 and 14YWT(PM2) irradiated to nominal 48 dpa with 47 appm He/dpa. Filled symbols are for nominal He/dpa (≈ 50 ± 10 appm) condition, while open symbols are from the shallower, open symbols with cross are from deeper locations.

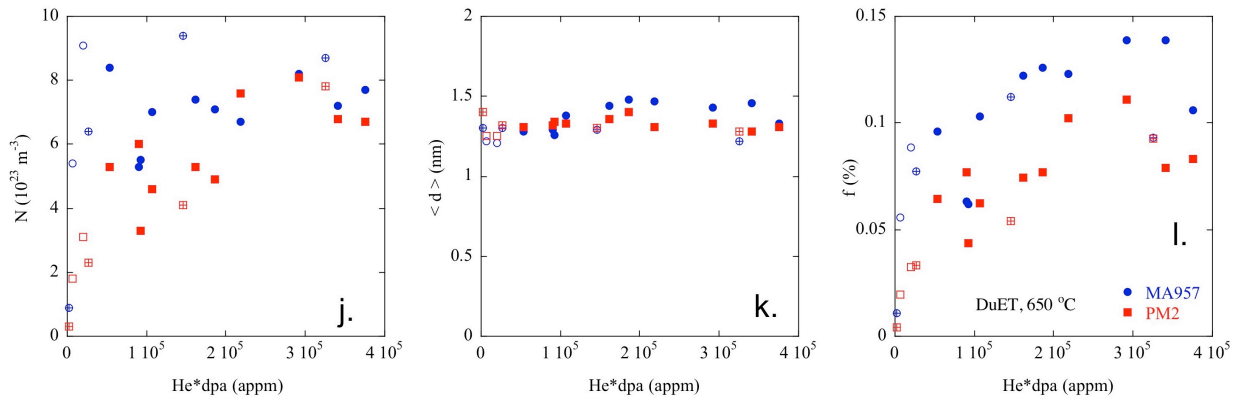


Figure 13j-l. The N, <d> and f of cavities as a function of the He*dpa for depths between 100 and 1600 nm in MA957 and 14YWT(PM2) irradiated to nominal 48 dpa with 47 appm He/dpa. Filled symbols are for nominal He/dpa (≈ 50 ± 10 appm) condition, while open symbols are from the shallower, open symbols with cross are from deeper locations.

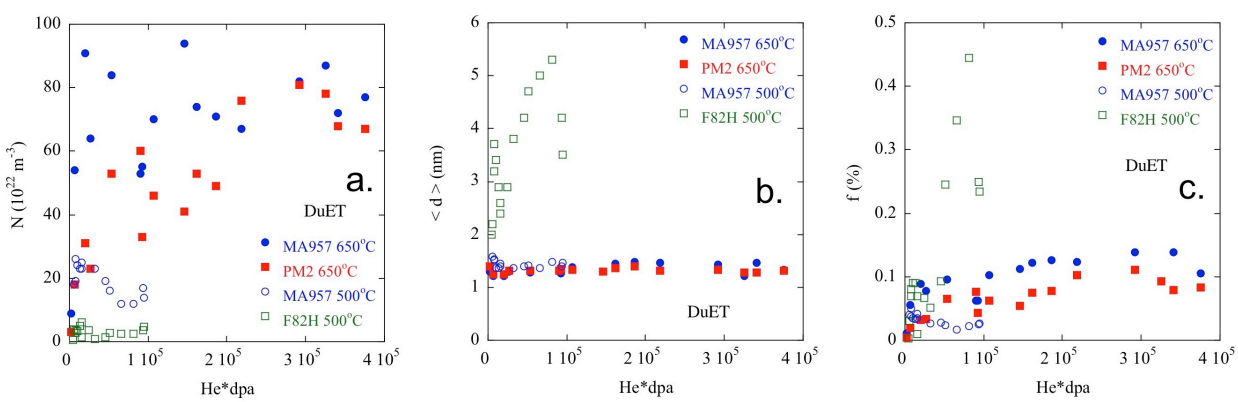


Figure 14. Comparison of all the DII results for N, <d> and f as a function of He*dpa.

**ACKNOWLEDGEMENTS**

The DII were conducted as a part of the TITAN program for US DOE- Japan MEXT collaboration for fusion energy research. The work performed at UCSB was supported by the U. S. Department of Energy, Office of Fusion Energy Sciences, under contract DE-FG03-94ER54275. We acknowledge the contributions of the NSF sponsored UCSB Microstructure and Microanalysis Facility. The ISHI results cited here were obtained as part of a collaboration with Drs. R. Kurtz and D. Edwards at PNNL and have been or will be discussed in detail in other publications.

**REFERENCES**


[1] Y. Dai, G. R. Odette, and T. Yamamoto, "*The Effects of helium on irradiated structural alloys," in* Comprehensive Nuclear Materials*, R. Konings, T. R. Allen, R. E. Stoller, and S. Yamanaka eds. (2012) Elsevier.*

[2] T. Yamamoto, G. R. Odette, and L. R. Greenwood, *Fusion Materials Semiannual Report 1/1 to 6/30/2005* DOE/ER-313/38 (2005) 95.

[3] T. Yamamoto, G. R. Odette, P. Miao, D. T. Hoelzer, J. Bentley, N. Hashimoto, H. Tanigawa, and R. J. Kurtz, *J. Nucl. Mater.* **367** (2007) 399.

[4] R. J. Kurtz, G. R. Odette, T. Yamamoto, D. S. Gelles, P. Miao, B. M. Oliver, *J. Nucl. Mater.* **367-370** (2007) 417.

[5] G. R. Odette, M. J. Alinger, and B. D. Wirth, *Annu. Rev. Mater. Res.* **38** (2008) 471.

[6] T. Yamamoto, G. R. Odette, P. Miao, D. J. Edwards, R. J. Kurtz, *J. Nucl. Mater.* **386-**388 (2009) 338.

[7] D. J. Edwards, R. J. Kurtz, G. R. Odette, and T. Yamamoto, *Fusion Materials Semiannual Report 12/31/2009* DOE/ER-313/47 (2010) 59.

[8] G. R. Odette, P. Miao, D. J. Edwards, T. Yamamoto, R. J. Kurtz, and Y. Tanigawa, *J. Nucl. Mat.* **417** (2011) 1001.

[9] E. H. Lee, J. D. Hunn, T. S. Byun and L. K. Mansur, *J. Nucl. Mater.* **280** (2000) 18.

[10] H. Kishimoto, K. Yutani, R. Kasada, and A. Kimura, *Fusion Eng. Des.* **81** (2006) 1045.

[11] R. Kasada, H. Takahashi, H. Kishimoto, K. Yutani, and A. Kimura, *Materials Science Forum* ***654-656*** (2010) 2791 (*doi:10.4028/www.scientific.net/MSF.654-656.2791).*

[12] T. Yamamoto, Y. Wu, G. R. Odette, K. Yabuchi, and A. Kimura, *Fusion Materials Semiannual Report 12/31/2010* DOE/ER-313/49 (2011) 1.

[13] K. Shiba, M. Enoeda, and S. Jitsukawa, *J. Nucl. Mater.* **329-333** (2004) 243.

[14] A. Kimura, R. Kasada, K. Morishita, R. Sugano, A. Hasegawa, K. Abe, T. Yamamoto, H. Matsui, N. Yoshida, B. D. Wirth and T. D. de la Rubia, *J. Nucl. Mater.* **307-311** (2002) 521-526.

[15] G. R. Odette, T. Yamamoto, H. J. Rathbun, M. Y. He, M. L. Hribernik, and J. W. Rensman, *J. Nucl. Mater.* **323** (2003) 313.

[16] T. Yamamoto, G. R. Odette, H. Kishimoto, J-W. Rensman, and P. Miao, *J. Nucl. Mater.* **356** (2006) 27.

[17] Z. Tong and Y. Dai, *J. Nucl. Mater.* **385** (2009) 258.

[18] M. L. Hamillton, D. S. Gelles, R. J. Lobsinger, M. M. Paxton, and W. F. Brown, "Fabrication Technology for ODS Alloy MA957", PNL-13165, Pacific Northwest Laboratory (2000).

[19] Y. Wu et al., to be published.

[20] A. Kohyama, Y. Katoh, M. Ando, and K. Jimbo, *Fusion Eng. Des.* **51-52** (2000) 789.

[21] G. R. Odette, T. Yamamoto, Y. Wu, E. Stergar, N. J. Cunningham, R. J. Kurtz, and D. J. Edwards, *Fusion Materials Semiannual Report 12/31/2011* DOE/ER-313/51 (2012) 91.